OPEN ACCESS

ARTICLE

The Innovation Materials

Ultrafast isothermal measurement of time-temperature-transition curve for critical nucleation in amorphous matrix

Hao-De Dong,[1,2,7] Ming-Xi Chen,[2,3,7] Peng Zhang,[4] Ming-Yang Qin,[1,2] Mei Shen,[2,5,*] and X.-D. Xiang[2,6,*]

*Correspondence: shenm@mail.sustech.edu.cn (M.S.); xdxiang@iphy.ac.cn (X.X.)

Received: April 15, 2025; Accepted: September 16, 2025; Published Online: October 11, 2025; https://doi.org/10.59717/j.xinn-mater.2025.100163

GRAPHICAL ABSTRACT

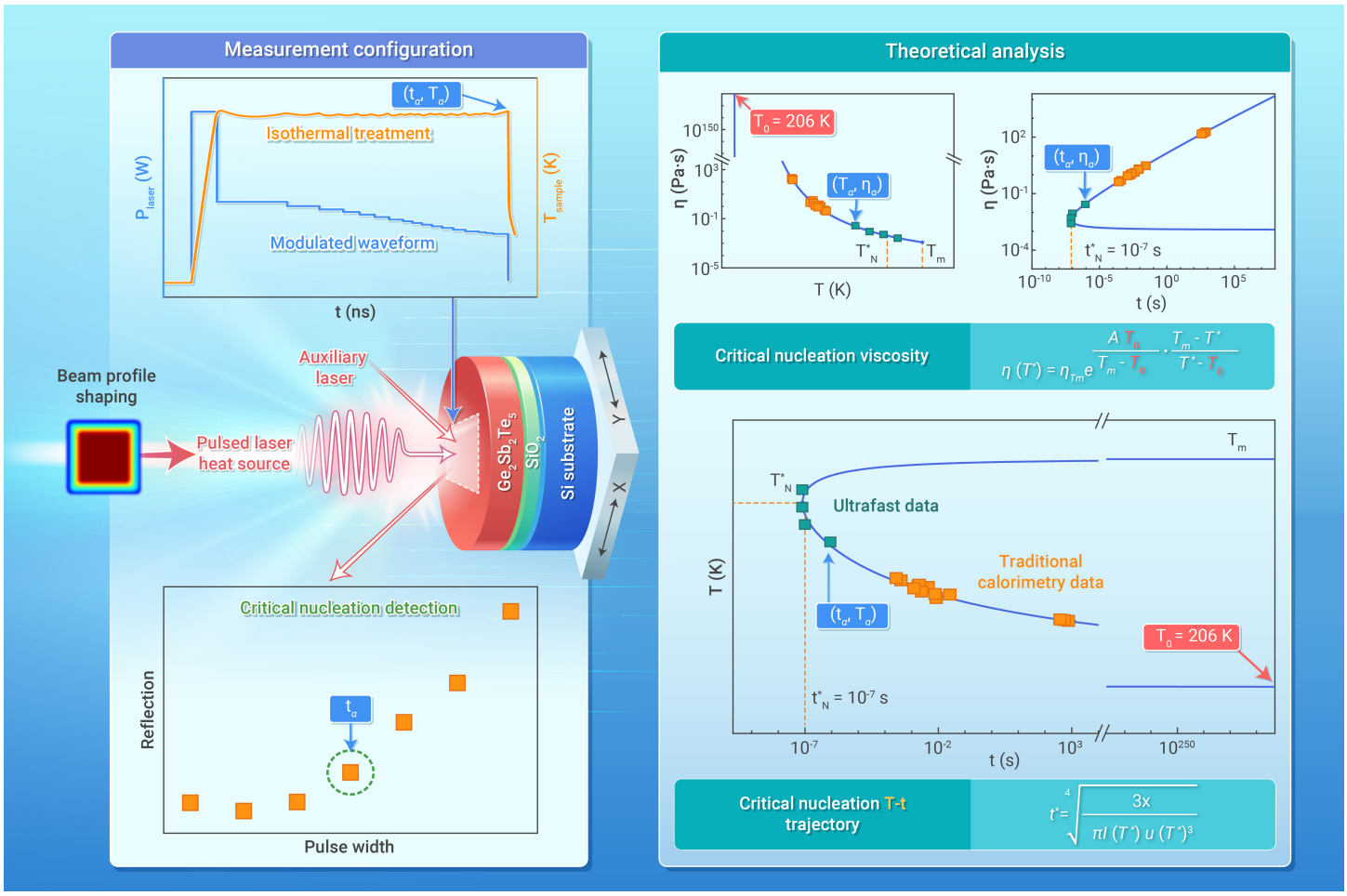

PUBLIC SUMMARY

- Ultrafast isothermal laser treatment shortens phase transition probing time by three orders of magnitude.
- Whether amorphous phases show a clear solid-liquid transition is a crucial 21st-century scientific question.
- Theoretical model extracts T_0—the boundary between amorphous liquid and solid for most materials.

ARTICLE

OPEN ACCESS

Ultrafast isothermal measurement of time-temperature-transition curve for critical nucleation in amorphous matrix

Hao-De Dong,[1,2,7] Ming-Xi Chen,[2,3,7] Peng Zhang,[4] Ming-Yang Qin,[1,2] Mei Shen,[2,5,*] and X.-D. Xiang[2,6,*]

[1]Institute of Physics, University of Chinese Academy of Sciences, Beijing 100190, China
[2]Department of Materials Science and Engineering, Southern University of Science and Technology, Shenzhen 518055, China
[3]Department of Mechanical Engineering, The Hong Kong Polytechnic University, Hong Kong SAR 999077, China
[4]Academy for Advanced Interdisciplinary Studies, Southern University of Science and Technology, Shenzhen 518055, China
[5]College of Integrated Circuits, Shenzhen Polytechnic University, Shenzhen 518052, China
[6]Institute of Physics, National Laboratory for Condensed Matter Physics, Chinese Academy of Sciences, Beijing 100190, China
[7]These authors contributed equally
*Correspondence: shenm@mail.sustech.edu.cn (M.S.); xdxiang@iphy.ac.cn (X.X.)

Received: April 15, 2025; Accepted: September 16, 2025; Published Online: October 11, 2025; https://doi.org/10.59717/j.xinn-mater.2025.100163

Citation: Dong H., Chen M., Zhang P., et al. (2025). Ultrafast isothermal measurement of time-temperature-transition curve for critical nucleation in amorphous matrix. *The Innovation Materials* **3**:100163.

The "nature of glassy substance", one of the top ten physics challenges of the century, requires understanding of non-equilibrium amorphous-to-crystalline phase transitions. The Time-Temperature-Transition (TTT) curve defines the critical phase transition conditions and offers a systematic framework to address this question. However, current TTT curve measurements are constrained by low heating rates (< 10^6 K/s), which limit data acquisition for most materials. This study developed an innovative pulsed laser isothermal heating method for in-depth TTT curve characterization. Heating rates exceeding 10^{11}K/s and isothermal durations ranging from 10^{-9} s to 10^{-5} s were achieved. A comprehensive Time–Temperature–Transition (TTT) curve, featuring a nose time t_N^* as short as 8×10^{-8} s, for the prototype phase-change memory material $Ge_2Sb_2Te_5$, was experimentally constructed, and key non-equilibrium thermodynamic properties were derived through quantitative TTT curve model analysis. Notably, the transition temperature T_0, which marks the quantitative boundary between the amorphous liquid phase and the amorphous solid phase, has been precisely determined for $Ge_2Sb_2Te_5$ as 206.54 K.

INTRODUCTION

In 2005, Science magazine highlighted the "nature of a glassy substance" as one of the top ten most profound physics questions of the century:[1] "Molecules in a glass are arranged similarly to those in liquids but are more densely packed. Where and why does the transition from liquid to glass occur?" This recognition prompted a series of long-standing debates,[2-4] including: (1) Is the glass state a liquid or a solid? (2) At what temperature does an amorphous liquid transition into an amorphous solid, analogous to the melting temperature of the crystalline phase? (3) Do all materials exhibit both amorphous and crystalline phases?

Despite the absence of discontinuities in thermodynamic parameters during the glass transition, recent studies on phase transition thermodynamics suggest that T_0, defined as the temperature at which atomic diffusion goes to zero, extracted from experimental time-temperature-transition (TTT) curves, can serve as a transition temperature between liquid and solid glass.[5]

However, answering the third question requires a new technique capable of measuring TTT for most materials. According to classical nucleation and growth theory, it is generally accepted that any molten material can become amorphous if cooled sufficiently rapidly.[6,7] For instance, monatomic tantalum currently holds the record for the highest known the critical cooling rate, reaching up to 10^{14} K/s.[8] However, the characterization techniques for the phase transition processes of amorphous materials, particularly for TTT curves, lag far behind the advancements in preparation technologies. Despite the identification of more than 4,000 amorphous materials, fewer than ten complete TTT diagrams have been established through isothermal experiments,[9-18] with the shortest observed nose time being only on the order of 10^{-2} s. Even in continuous heating experiments, the shortest recorded transformation time is still limited to the order of 10^{-4} s.[19] This limitation hinders progress in determining the critical transition conditions (T^*, t^*) near the nose temperature T_N^* and nose time t_N^*,[5] consequently restricting the precise determination of the key parameter T_0 and impeding the understanding of these fundamental issues in physics and materials science.

Quantitative analysis of TTT curves also guides processes such as (1) the nanoscale superplastic forming of amorphous materials,[20,21] (2) the precise control of nanocrystals within amorphous matrices, (3) the research on microstructural and dynamic inhomogeneities in amorphous systems,[22,23] and (4) the investigation of localised thermal and transport properties in amorphous systems.[24,25]

Characterization of TTT curves, which requires isothermal crystallization of amorphous materials, is typically performed using calorimetric techniques, such as differential scanning calorimetry (DSC), differential thermal analysis (DTA), Flash-DSC and Nano-DSC.[19,26,27] These techniques achieve typical heating and cooling rates of 10^6 K/s to 10^{-2} K/s, which are significantly slower than the nucleation rates at the noses of TTT curves for most materials. Moreover, traditional approaches to investigate the interplay between temperature and time during the critical nucleation processes are further limited by the inherent complexity of amorphous states and challenges in the characterization of isothermal crystallization of amorphous materials on ultrafast time scales. Therefore, technological advancements are called for to meet these requirements.

In recent years, advancements in ultrafast heat treatment and measurement techniques have opened new avenues for probing the nucleation thermodynamics, enabling researchers to capture transient states with unprecedented precision. Electrical and optical pulse stimuli techniques are commonly used for rapid heating or cooling, with optical pulses offering distinct advantages. Optical pulses enable contactless heating, provide precise energy confinement due to the high directivity of laser beams, and offer faster response times, thereby minimising thermal conduction to unirradiated regions.

Currently, non-destructive optical reflectance measurements have become a robust tool for high-throughput characterization[28-31] of thermophysical properties as well as ultrafast transient measurements[32,33] of transport properties. For phase change materials (PCMs), a > 30% reflectance change—corresponding to a resistivity variation over 3 orders of magnitude—allows precise quantitative monitoring of phase transitions via optical reflectivity.[34-36] $Ge_2Sb_2Te_5$ is widely regarded as a representative and well-studied PCM, essential for advancing next-generation non-von Neumann artificial neural networks (ANNs).[37,38] Pulsed lasers with various time scales including nanoseconds, picoseconds, and femtoseconds, have been employed to investigate phase transition thermodynamics of $Ge_2Sb_2Te_5$. Picosecond pulsed lasers can achieve rapid cooling rates of up to 10^{13} K/s, effectively inhibiting the nucleation and growth of crystalline phases in high purity metal targets and facilitating the formation of stable amorphous monatomic metal nanoparticles.[39] Huang Huan et al. and Alexey V. Kiselev et al. investigated the phase transition behaviour of $Ge_2Sb_2Te_5$ films induced by microsecond and nanosecond pulsed lasers, quantifying the crystallization and amorphous transition times and rates.[40,41] Y. Liu et al. studied the crystallization of $Ge_2Sb_2Te_5$ using a series of femtosecond multi-pulsed lasers and developed a heat transfer model to quantify the growth rate.[42] Jia Du et al. examined the

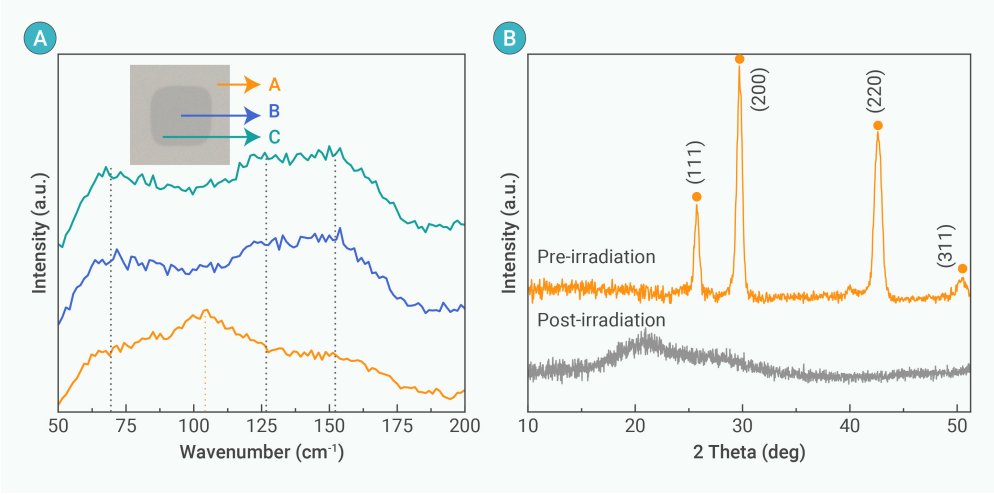

Figure 1. Phase structure characterization and amorphous/crystalline identification of $Ge_2Sb_2Te_5$ (A) Raman spectrum for the amorphous and crystalline state of $Ge_2Sb_2Te_5$. The inset shows an optical microscopic image of a single-shot laser irradiated area. (B) X-ray diffraction (XRD) patterns of $Ge_2Sb_2Te_5$ films in the crystalline phase and the laser-induced amorphous phase.

multiple intermediate states of $Ge_2Sb_2Te_5$ induced by nanosecond pulsed lasers and investigated how laser parameters affect crystallinity.[43] Liu et al. developed a 3D finite element model for pulsed laser processing of $Ge_2Sb_2Te_5$ films, analysing the effects of parameters on the temperature field.[44] Xiang et al. developed a "one-chip method" for rapidly constructing the phase diagram of $Ge_xSb_xTe_{1-x-y}$ crystallization temperatures by scanning the film point-by-point with nanosecond pulsed lasers.[45]

However, all previous studies on laser-induced phase transition thermodynamics of PCMs do not implement precise thermal field regulation or even temperature control, and research on laser-induced isothermal phase transition behaviour for constructing TTT curves remains largely unexplored. V. Weidenhof et al. characterised isothermal crystallization in $Ge_2Sb_2Te_5$ films by monitoring the reflectivity of pulsed lasers, but their data were limited to the time scale of tens of seconds.[46] The isothermal characterization of the TTT curve for time durations $< 10^{-5}$ s remains unexplored due to the challenges in achieving ultrafast isothermal heating conditions.

In this study, $Ge_2Sb_2Te_5$ deposited on a silicon wafer was selected as the target material. Using a pulsed laser isothermal heating system combined with finite element simulations, we investigated (i) the critical pulse widths at various laser powers required to trigger melting of the crystalline phase and subsequent rapid quenching into the amorphous phase, and (ii) the fine-tuned pulsed laser waveforms necessary for isothermal heating of $Ge_2Sb_2Te_5$. The experimental data obtained in this study, along with those acquired from calorimetric techniques, were successfully fitted to a phenomenological model of the TTT curve with only three unknown parameters. Transition temperature $T_0 = 206.54$ K from an amorphous liquid to an amorphous solid was obtained for $Ge_2Sb_2Te_5$. Nose temperature t_N^* for $Ge_2Sb_2Te_5$ is determined to be 8×10^{-8} s. This technique and method provide a clear pathway to reveal the nature of the glassy state across a broad range of materials.

MATERIALS AND METHODS

Sample preparation and characterization

$Ge_2Sb_2Te_5$ thin films were deposited onto silicon substrates using the magnetron sputtering module of the PRO Line PVD 75 system (Kurt J. Lesker Co.) with a stoichiometric $Ge_2Sb_2Te_5$ alloy target. Deposition was carried out under 3 mT magnetic field and 50 sccm flowing Ar atmosphere at 30 W for 30 mim. Following deposition, the films underwent rapid thermal processing (Hefei Kejing, OTF-1200X-4 system) at 200°C under a flowing Ar atmosphere for 30 min, converting the amorphous thin film into the cubic crystalline structure.

To ensure both the accuracy and uniformity of the film composition, several symmetrically distributed positions across the wafer surface were selected for energy-dispersive X-ray spectroscopy (EDX) analysis. The results confirmed an average composition of Ge:Sb:Te ≈ 22.96:23.75:53.29 at%, as shown in Table S1, which closely matches the nominal composition of $Ge_2Sb_2Te_5$ (22:22:56 at%) and indicates a uniform elemental distribution throughout the film.

Ellipsometry analysis of the annealed film was conducted to examine the film thickness and uniformity across the wafer surface. Measurements were performed at four symmetrically distributed positions, revealing a layered structure composed of an approximately 18.5 nm $Ge_2Sb_2Te_5$ layer (see Table S1) atop a 2 nm native SiO_2 layer on the Si substrate. Thickness measurements taken using a stylus profilometer (KLA, Alpha Step D-300) consistently yielded an average thickness of 18 nm. The close agreement between the two techniques confirms the high uniformity of the deposited film.

The ellipsometry data were analysed using the General Oscillator (Gen-Osc) model to derive the optical properties of the $Ge_2Sb_2Te_5$ film prior to laser irradiation. These properties were subsequently applied in finite element simulations for the amorphous phase transition. The extracted optical constants of the $Ge_2Sb_2Te_5$ crystalline phase—including the refractive index (n), extinction coefficient (κ), absorption coefficient (α), and reflectance (R)—over the wavelength range of 245-1690 nm are shown in Figure S1. The values of α and R at 1064 nm are listed in Table S2.

To examine the crystalline structure of the $Ge_2Sb_2Te_5$ film prior to laser irradiation, Raman[47-49] and X-ray diffraction[49-52] measurements were carried out using a Renishaw in-Via Qontor and a Rigaku SmartLab system, respectively. The Raman spectra obtained from inside and outside the region irradiated by a single point mono pulse laser are shown in Figure 1A, with optical microscopic images in the inset. The distinct peak observed at 105 cm^{-1} in the Raman spectra of spot "A" located outside the laser-irradiated region, is attributed to the A_1 mode of $GeTe_4$ corner-sharing tetrahedra, indicating the crystalline structure of the $Ge_2Sb_2Te_5$.[47-49] Grazing incidence X-ray diffraction (XRD) measurements performed on the $Ge_2Sb_2Te_5$ films are shown in Figure 1B. The pre-irradiated film exhibited sharp diffraction peaks corresponding to the FCC phase (space group: Fm-3m).[49-52]

Pulsed laser-induced amorphous phase transition

Beam profile optimization for uniform surface processing. To facilitate the pulsed laser-induced phase transition process of the $Ge_2Sb_2Te_5$ film, we developed a pulsed laser isothermal heating system (PLIHS). Details of the PLIHS design and testing are provided in the Section "Pulsed Laser Isothermal Heating System".

It should be emphasized that real-time monitoring of phase-change processes remains inherently challenging due to their transient and non-equilibrium nature. Techniques capable of capturing "single-shot, transient" parameters during such events remain experimentally demanding and beyond current practical reach.[53-58] To address this limitation, we employed a spatially separated, multi-spot laser heating approach, which, when combined with stepwise parameter tuning and post-process reflectivity analysis, enabled effective monitoring of phase-change events.

Most commercial laser micro-processing systems use beams with a Gaussian profile, which exhibit an uneven intensity distribution across the cross-section, as shown in Figure 2A. On the one hand, this uneven distribution results in energy loss in the peripheral areas, where the low power (< 37% of the centre value) is insufficient to induce phase transition. On the other hand, the high central power, combined with a significant power gradient (approximately 63% power difference between the centre and edge), leads to severe material ablation and vaporisation. In contrast, the top-hat beam offers a more uniform lateral energy distribution, as shown in Figure 2A. The power fluctuation within the irradiated area of the top-hat beam is kept within ± 9.5%, with a sharp power drop at the boundary, showing a power difference of > 90%. Furthermore, the top-hat square beam profile eliminates the uneven

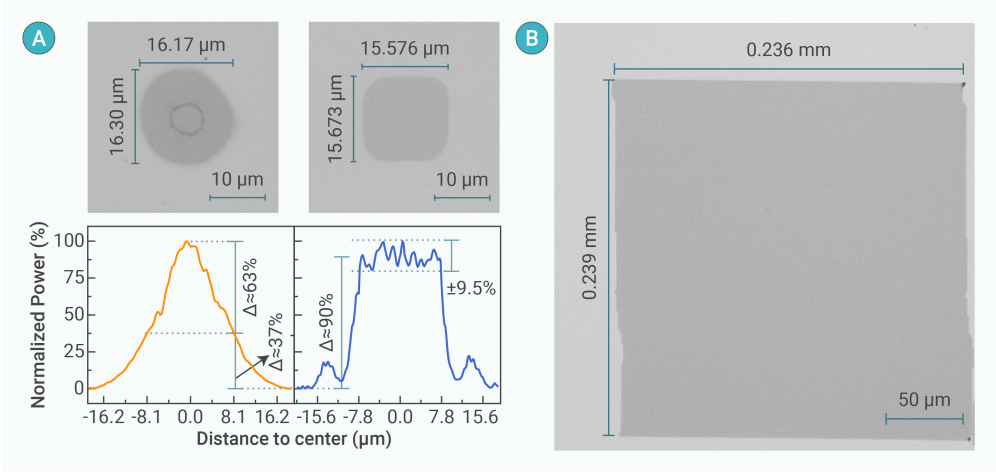

Figure 2. Demonstration of laser beam cross-sectional energy homogenization (A) One-dimensional energy profiles of Gaussian and top-hat laser beams obtained using a beam profiler, normalized to their respective maxima, and the corresponding optical micrographs of irradiated micro area on the film surface. (B) An optical microscopic image of laser scanning large-area amorphous region.

overlap issue typical of Gaussian beams, enabling seamless large-area laser processing via point-by-point scanning, as demonstrated in Figure 2B.

To optimize the energy distribution of the beam, a beam shaper (ST-291-I-Y-A, HOLOOR) was introduced in the PLIHS system. It converts a Gaussian beam profile into a top-hat square beam profile along the beam propagation path. This beam shaper is coupled with an objective lens in front of the sample stage to tune the focused spot size.[59,60] Under optimized conditions (such as pulse power and duration; details provided in Section "Critical Pulse Widths for Amorphous Phase Transition"), the beam shaper can achieve uniform surface modification of the irradiated area by evenly distributing the energy across the beam's cross-section.

Construction of finite element simulation model. While the PLIHS serves as a reliable platform for laser processing, real-time temperature monitoring during laser processing at nanosecond temporal and micrometre spatial scales remains a significant challenge. To address this, we employed finite element simulation to model heat transfer in a $Ge_2Sb_2Te_5$ film under pulsed laser irradiation, which enables the quantification of temperature evolution during pulsed laser irradiation.

The geometric model comprised an 18-nm-thick $Ge_2Sb_2Te_5$ layer atop a 2nm SiO_2-capped 40-μm-thick Si substrate. Material properties, including thermal conductivity (λ), density (ρ) and specific heat capacity (C_p), were obtained from the literature[61-65] and listed in Table S2. All materials were assumed to be thermally isotropic. The pulsed laser source was modelled as a top-hat square beam with a wavelength of 1064 nm. The film's top surface was cooled by air without forced convection, with an ambient temperature fixed at 293 K. The temperature (T) versus time (t) curve was extracted from the centre of the laser-irradiated region.

The Beer-Lambert law was applied to simulate laser beam absorption along the z-axis of the film. This law is valid for perpendicular incidence of parallel monochromatic light on the surface of a uniform medium, assuming no refraction, scattering, or other interactions. The laser intensity decreases to a fraction of its initial value at a specific depth beneath the surface, as expressed by the following equation:[66]

$$I = I_0(1-R)e^{-\alpha z}, \tag{1}$$

where I is the local laser energy density, I_0 is the initial incident laser energy density, R is the reflectivity, α is the attenuation coefficient, z is the z-axis depth from the surface.

The heat transfer field within the film was simulated using the following partial differential equation:[67]

$$Q = \rho C_p \frac{\partial T}{\partial t} - \nabla \cdot (\lambda \nabla T) + \rho C_p v \cdot \nabla T, \tag{2}$$

where Q is the external heat input, ρ is the density, C_p is the specific heat capacity, T is the temperature, t is the time, λ is the thermal conductivity, and v is the velocity vector under Euler coordinates. Moreover, $\rho C_p \frac{\partial T}{\partial t}$ represents the transient (or heat storage) term, $-\nabla \cdot (\lambda \nabla T)$ corresponds to the conduction term, $\rho C_p v \cdot \nabla T$ is the convective term (which vanishes in solids since $v = 0$). By equating I to Q in the above equations, the coupling between the laser field and the heat transfer field was established.

Critical pulse widths for amorphous phase transition. It is worth noting that simulations were limited to temperatures at or below the melting point of $Ge_2Sb_2Te_5$, focusing on the critical melting and isothermal conditions. Simulations above the melting point were avoided due to both the scarcity of experimental data on melt-state properties of $Ge_2Sb_2Te_5$ and the intrinsic complexity of the liquid phase. In particular, the significantly high optical absorption of the molten state renders the Beer-Lambert-based laser field model (**Eq. 1**) invalid, as most of the laser energy is absorbed at the surface and cannot penetrate deeper—an undesirable effect. Thus, exploring definitive optimal pulse width and power parameters for the "critical state"—where the temperature-time evolution completes heating and achieves thermal equilibrium at the melting point (888 K[61]) without overshooting the temperature—is essential for pulsed laser-induced amorphous phase transition. This definition of the critical state ensures a high-quality amorphous phase transition region while preventing ablation or film damage.

A series of finite element simulations for $Ge_2Sb_2Te_5$ with varying pulse powers and widths were conducted to optimize laser parameters for the heating, thermal equilibrium at the melting point (888 K),[61] and subsequent cooling for amorphous phase transition. As shown by the gray line in Figure 3A, a laser pulse with insufficient power (5.2 W) requires 6 nsto reach T_m, with heat conduction dominating the temperature evolution. This is evident from the sudden slowdown in the temperature rise, where thermal conduction significantly reduces the heating rate. Such behaviour should be avoided, particularly for materials undergoing ultrafast phase transitions. Conversely, a laser pulse with sufficient power (6.1 W) allows the temperature to reach T_m smoothly within 2.02 ns (yellow line in Figure 3A). The latent heat stabilises the temperature until 2.90 ns (blue line in Figure 3A), which is considered the critical pulse width at 6.1 W. If the pulse width exceeds 2.90 ns, the surface temperature rises above the melting point, as illustrated by the green line in Figure 3A, potentially causing material ablation.

At the critical pulse width for a specific pulse power, a thermal equilibrium state is reached at the melting point, where the temperature remains constant. Figure 3B shows the finite element simulation results for various pulse widths and powers under the critical conditions. The data indicate that the critical pulse width decreases as pulse power increases. Higher pulse powers with shorter critical pulse widths are preferred for amorphous phase transition, as they enable faster cooling to room temperature.

The waveform editing capability of PLIHS allows precise control over the temporal and spatial thermal field distribution by adjusting the pulsed laser's falling edge, enabling flexible cooling rate regulation. For example, by shaping the falling edge into one or more slopes on a 7.9 W, 1.11 ns square waveform, finite element simulations produced temperature-time curves with varying cooling rates, as shown in Figure 3C. The linearity of these cooling curves can be further improved through finer waveform adjustments using advanced control theory. Precise cooling rate control optimises amorphous material formation, refines microstructures, and enhances physical and functional properties.

Characterization of laser-induced amorphous phase. Based on the simulation results under the critical condition (pulse power 6.1 W and pulse width 2.90 ns), a single-point mono-pulsed laser treatment using PLIHS was applied to the $Ge_2Sb_2Te_5$ film. Subsequently, the $Ge_2Sb_2Te_5$ film underwent point-by-point pulsed laser irradiation, producing a large-area, gapless phase transition region. Optical microscopy images of the single-point amorphized

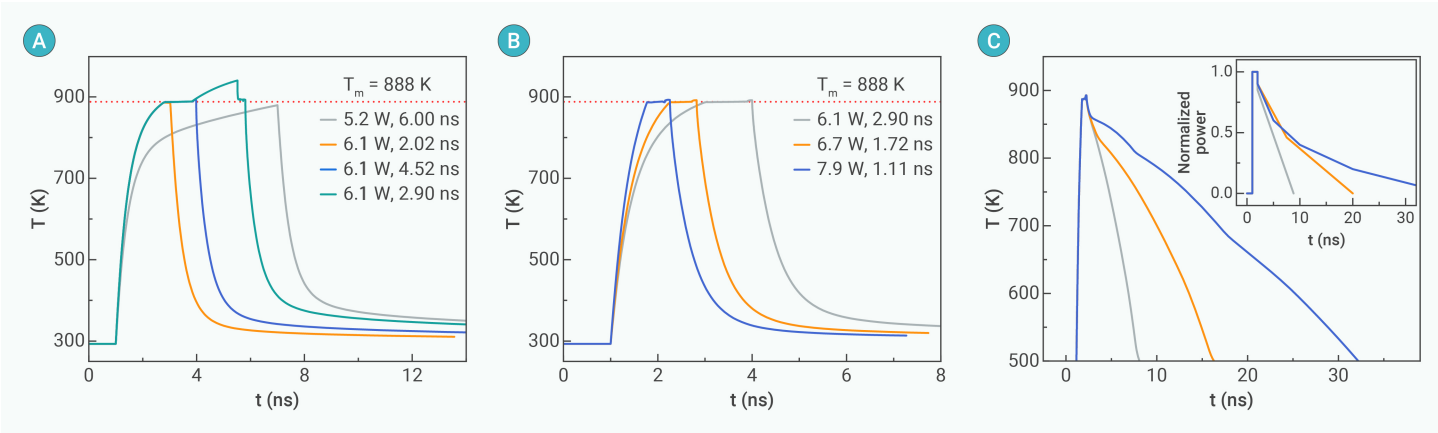

Figure 3. Finite element simulation of temperature-time evolution to investigate the optimal parameters for pulsed laser-induced amorphization of $Ge_2Sb_2Te_5$ (A) Simulated temperature-time ($T-t$) curves for various laser pulse powers and pulse widths. (B) Simulated $T-t$ curves showing the critical pulse widths for various pulse powers. (C) Simulated $T-t$ curve of different cooling rates and their corresponding pulsed laser waveforms in the inset.

micro area and the large-area amorphized region are shown in Figures 2A-B, respectively.

To confirm the phase change characteristics of the laser-irradiated regions, Raman[47-49] and XRD[49-52] analyses were conducted on both the single-point irradiated micro area and the large-area irradiated region. The Raman spectrum of spots "B" and "C" shown in Figure 1A within the laser-irradiated region reveals distinct peaks at approximately 74 cm^{-1}, 125 cm^{-1} and 150 cm^{-1}, corresponding to the E mode of $GeTe_4$ tetrahedra, the A_1 mode of $GeTe_{4-n}Ge_n$ (n = 0, 1, 2) tetrahedra, and the Sb-Te bond vibration of Sb_mTe_3 (m = 1, 2), respectively, indicating the amorphous nature of the $Ge_2Sb_2Te_5$ film.[47-49] The XRD spectrum of laser-irradiated film, shown in Figure 1B, displays a broad amorphous diffraction hump, indicating that the film underwent melting followed by rapid quenching. A distinct phase contrast between the irradiated and non-irradiated regions was confirmed, with uniform amorphous phase transition observed within the irradiated regions and crystalline characteristics in the surrounding area.

In addition, ellipsometry characterization of the large-area phase transition region provided spectra for the refractive index (n), extinction coefficient (κ), attenuation coefficient (α), and reflectance (R) of the $Ge_2Sb_2Te_5$ film. These spectra, detailed in Figure S1 & Table S2, further demonstrate the pronounced difference between the amorphous and crystalline states, while also providing input parameters for finite element simulation.

Pulsed laser-induced isothermal heat treatment

Pulsed laser isothermal heating system. When using a pulsed laser as a heat source for precise isothermal thermal treatment of a sample, a dynamic balance between heat absorption and heat dissipation must be maintained. This requires complex waveforms rather than simple square waves, with precise time control.

Therefore, a pulsed laser isothermal heating system (PLIHS), shown in Figure 4A, was developed to achieve precise temporal control for isothermal heating. A 1064 nm pulsed laser system (MOPAW-AWG, INO) served as the heat source. A Master Oscillator Power Amplifier (MOPA) system provides coarse temporal control at a resolution of 1 ns. A high-frequency arbitrary waveform generator (AWG) operating at nearly 8 GHz provides fine temporal control with a 130 ps resolution, modulating the intensity of a semiconductor seed diode.[68] Overall, the laser source configuration, as shown in Figure 4A, enables the generation of programmable, complex amplitude waveform pulsed lasers with adjustable pulse widths ranging from 130 ps to 4 μs.

To assess the time resolution of the PLIHS output, the laser pulse waveform was measured using an ultrafast photodetector and a high-speed oscilloscope, as shown in Figure 4B. The quality was evaluated by the rise time, fall time, and a quality factor defined as the ratio of the flat-top area to the total pulse area. As shown in Table S3, the PLIHS features edge transitions on the order of 1 ns, and near-ideal rectangularity with a quality factor close to 1, indicating that the time resolution is sufficient for our experiment.

A 632 nm visible He-Ne laser (HNL150RB, THORLABS) was introduced into the PLIHS system for in situ monitoring of reflected light signal, coupled with an ultrafast InGaAs PIN photodetector (UPD-15-IR2-FC, ALPHALAS, with a pulse repetition frequency range from DC to 25 GHz, a rise time shorter than 15 ps) and a high-speed oscilloscope (MSO64B, Tektronix, with a bandwidth ranging from 1 GHz to 10 GHz and a maximum sampling rate of 50 GS/s). The detection beam was aligned coaxially with the heating beam to ensure reliable acquisition of reflected signals from the heated area. The PLIHS system also integrates a mechanical sample stage (LTVH-100, AML) with stepwise motion, which can be precisely synchronised with individual laser pulses, enabling large-area scanning for amorphous phase formation.[60]

Calibration of melting temperature in finite element simulation. The critical conditions for laser-induced amorphous phase transition were explored in the previous section "Critical Pulse Widths for Amorphous Phase Transition". For the laser-induced crystallization process, the key point lies in the accuracy of the temperature output from the finite element simulation for specific laser waveforms, which determines the time-temperature coordinates of the final TTT data. To validate the reliability of the finite element model in simulating temperature, specifically to calibrate the model, we selected the measured melting temperature of 888 K from this study and from the literature[61] to calculate the heat transfer process during pulsed laser irradiation.

Within the laser-irradiated micro area of $Ge_2Sb_2Te_5$ layer, three primary forms of heat are identified: sensible heat (Q_{sen}), which causes a temperature increase limited by the material's specific heat capacity; latent heat (Q_{lat}), which results in a temperature plateau around the melting point; and heat transferred to the surroundings, primarily through conduction (Q_{cond}), with less contributions from convection (Q_{conv}) and radiation (Q_{rad}). Given the complexity of heat transfer during material melting and the lack of relevant material properties, we focus on calculating the time interval t_{sen}, from the onset of pulsed laser irradiation to the onset of melting. The latent heat Q_{lat} is neglected during t_{sen}. According to the principle of energy conservation, we have:

$$Q_{source} \approx Q_{sen} + Q_{cond} + Q_{conv} + Q_{rad}. \tag{3}$$

Each energy term is calculated using the following equations:

$$Q_{source} = P \cdot t_{sen} \cdot (1-R) \cdot (1-\exp(-\alpha \cdot z_{GST})), \tag{4}$$

$$Q_{sen} = \int_0^{z_{GST}} (T(z) - T_{ini}) \cdot C_p(T) \cdot \rho \cdot S \cdot dz, \tag{5}$$

$$Q_{cond} = \int_{t_{sen}} I_{hf}(t) \cdot S_{hf} \cdot dt, \tag{6}$$

$$Q_{conv} = \int_{t_{sen}} h \cdot (T(t) - T_{amb}) \cdot S \cdot dt, \tag{7}$$

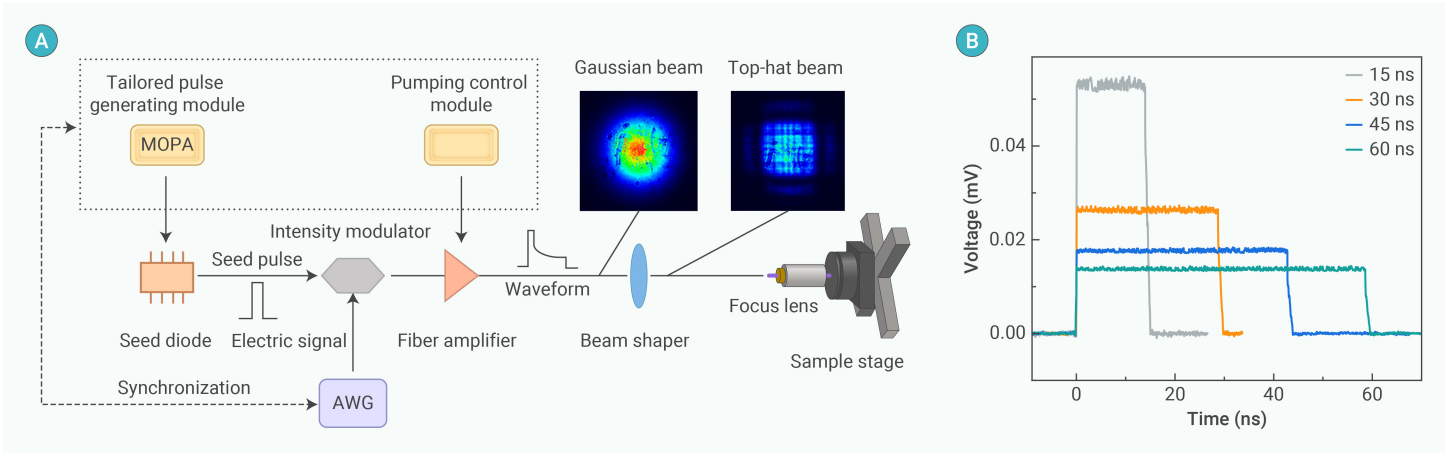

Figure 4. PLIHS experimental setup and performance characteristics (A) A schematic diagram of the PLIHS. (B) Comparison of PLIHS output waveforms at different pulse durations with fixed pulse energy.

Table 1. Various calculated energy terms during laser irradiation.

P (W)	t_{sen} (ns)	Q_{sen} ($\times 10^{-10}$ J)	Q_{cond} ($\times 10^{-10}$ J)	Q_{rad} ($\times 10^{-16}$ J)	Q_{conv} ($\times 10^{-13}$ J)	Q_{source} ($\times 10^{-9}$ J)	Relative error (%)
6.1	2.020	5.747	16.270	1.185	1.728	2.098	4.75
6.7	1.276	5.215	9.879	0.602	0.921	1.455	3.59
7.9	0.774	5.121	5.767	2.150	2.512	1.041	4.39

$$Q_{rad} = \int_{t_{sen}} \sigma \cdot \varepsilon \cdot \left(T(t)^4 - T_{amb}^4\right) \cdot S \cdot dt, \quad (8)$$

where P is the instantaneous laser power, R is the reflectivity, a is the attenuation coefficient, z_{GST} is the thickness of the $Ge_2Sb_2Te_5$ film, $C_p(T)$ is the specific heat capacity, ρ is the density and S is the area of the laser-irradiated micro area. $I_{hf}(t)$ represents the heat flux in the laser-irradiated micro area, encompassing both conduction loss towards the bottom and conduction loss towards the non-laser-irradiated area. S_{hf} is the corresponding heat dissipation interface area, h is the heat transfer coefficient, $\sigma = 5.670 \times 10^{-8}\ \mathrm{W \cdot m^{-2} \cdot K^{-4}}$ is the Stefan–Boltzmann constant, and ε is the emissivity. $T(z)$ is the temperature distribution across the depth profile, and $T(t)$ is the time evolution of the mean surface temperature. T_{ini} is the initial temperature, and T_{amb} is the ambient temperature, with the condition $T_{ini} = T_{amb} = 293.15\mathrm{K}$.

The temperature distribution is uniform along the in-plane direction, but exhibits a significant gradient along the z-axis direction. In these calculations, the central temperature is approximated as the mean in-plane temperature, considering only the temperature variation along the z-axis. The calculation results for three sets of laser parameters are listed in Table 1, indicating that the discrepancy between the input energy from the pulsed laser and the sum of sensible heat and dissipated heat in the laser-irradiated micro area is within an acceptable range. This discrepancy may arise from the idealised assumption that the central temperature represents the mean in-plane temperature, as well as from the sharp temperature drop at the edge of the irradiated area. The calculations are based on time-temperature curve data from the simulation model and well-verified melting point data. The acceptable relative error confirms the accuracy and feasibility of the simulation model.[61]

Moreover, material properties in the finite element simulations were partially obtained from the literature, with discrepancies among reported values arising from variations in experimental conditions. Therefore, an error analysis was conducted to assess the influence of parameter uncertainties on key simulation results, including the pre-melting time interval and the critical pulse width. Reported values of density,[51,52,62,69,70] specific heat capacity,[19,62,65,71-74] and thermal conductivity[50,64,74-81] for $Ge_2Sb_2Te_5$ thin films were compiled, and the resulting error ranges of the output parameters are discussed in Figures S2-S3 & Table S4. It is important to note that the purpose of the error analysis is solely to emphasize the uncertainty in simulation results arising from the parameters reported in the literature. By calibrating the simulation model with the known melting point through energy conservation calculations, the optimal parameters have been clearly identified, aligning precisely with the experimental results, and thus avoiding uncertainties introduced by literature-based parameters.

Pulsed laser-induced critical isothermal crystallization. Before characterizing the crystallization thermodynamics, PLIHS was used for large-area pulsed laser scanning on $Ge_2Sb_2Te_5$ films to create an amorphous precursor film (a-$Ge_2Sb_2Te_5$). Subsequently, to achieve isothermal heating of the a-$Ge_2Sb_2Te_5$ films, a staircase falling edge laser waveform was designed, utilizing PLIHS's programmable amplitude capabilities along with temperature outputs from finite element simulations. At a specific laser power, the material's temperature increases continuously. Once the target temperature is reached, the laser power must be appropriately reduced to maintain a stable temperature. Achieving thermal equilibrium over extended periods requires a staircase waveform with progressively decreasing laser power.

Figure 5A illustrates a typical isothermal platform at 800 K for 200 ns, achieved using a staircase waveform calibrated from finite element simulation. Laser waveforms of varying power (reflecting different thermal treatment temperatures) were calibrated based on the critical amorphous phase transition condition, where the power is normalized to 6.1 W (left axis of Figure 5A). The figure details the waveform design and temperature evolution during the initial stage on a logarithmic time scale. Isothermal platforms at 750 K, 700 K, 650 K, and 600 K were similarly simulated using corresponding staircase waveforms with durations of up to 2000 ns.

Specific staircase waveforms were then applied to the a-$Ge_2Sb_2Te_5$ film surface in a point-by-point manner, with progressively increasing isothermal durations. For isothermal heating experiments at 800 K, 750 K, and 700 K, ten pulse widths were tested, ranging from 20 ns to 200 ns. For experiments at 650 K and 600 K, 20 pulse widths were tested, ranging from 100 ns to 2000 ns.

As shown in the inset of Figure 5B, a bright crystalline region emerges within the darker amorphous background when the phase transition occurs. A noticeable increase in reflectivity marks the phase transition, enabling precise determination of the critical nucleation conditions. At shorter pulse durations, the reflectivity remains nearly constant within a narrow range (approximately 0.429-0.433), indicating the amorphous incubation stage. Around the critical pulse duration and beyond, the reflectivity begins to

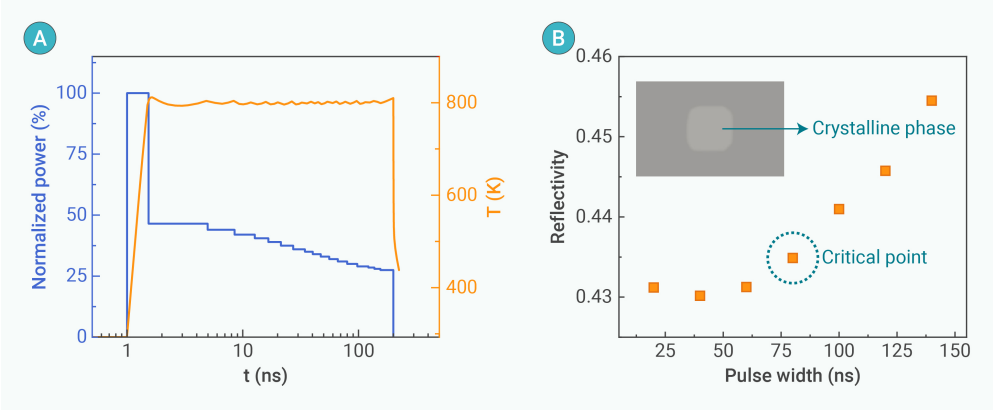

Figure 5. Isothermal laser heating strategy and optical crystallization identification (A) Simulation of a 200 ns staircase laser waveform for an 800 K isothermal platform. (B) Reflectivity versus pulse width for 750 K isothermal heating of a-$Ge_2Sb_2Te_5$. The inset shows a typical optical microscopy image of the laser-induced crystallized phase on the amorphous matrix.

exceed this stable baseline and subsequently exhibits an approximately linear increase, suggesting the onset and progression of crystal nucleation. This allows us to distinguish quantitatively between low, constant reflectivity and linearly increasing reflectivity regimes—serving as the basis for determining the critical nucleation condition at each temperature. For example, Figure 5B shows that during isothermal heating at 750 K, the reflectivity of a-$Ge_2Sb_2Te_5$ begins to increase distinctly at a pulse width of 80 ns, identifying it as the critical nucleation time at this temperature. Reflectivity data for various tested laser heating conditions are listed in Table S5. The critical nucleation times for 800 K, 700 K, and 650 K are 80 ns, 100 ns, and 900 ns, respectively. At 600 K, the critical nucleation time exceeds the operational limit of PLIHS. Furthermore, the above phase-change detection method avoids the need for real-time reflectivity monitoring, relying solely on pre- and post-irradiation measurements—enhancing robustness and applicability across diverse experimental settings.

RESULTS AND DISCUSSIONS

The TTT data obtained in this study are plotted in the time-temperature domain as green dots in Figure 6A. For comparison, the calorimetry data extracted from the literature are also included as yellow dots.[19] A phenomenological model is used to establish the quantitative relationship between the critical nucleation time (t^*) and the critical nucleation temperature (T^*), with the fitted TTT theoretical curve shown in Figure 6A as the blue solid line. In the figure, the crystallization temperature T_x is taken as 423 K,[61] the glass transition temperature T_g as 383 K,[82] and the melting point T_m as 888 K.[35] The smooth connection between the two datasets validates the feasibility of this novel isothermal crystallization thermodynamic characterization method.

The theoretical model is described by Eqs. 9-13, with definitions of all thermodynamic parameters provided in Table S6.[5,83-85]

$$t^* = f(T^*) = \sqrt[4]{\frac{3x}{\pi I(T^*)u(T^*)^3}}, \tag{9}$$

$$u(T^*) = \frac{k_B T^*}{3\pi}\frac{v}{\delta^2 \eta(T^*)}\left(1 - e^{-\frac{V_m \Delta g_v}{RT^*}}\right), \tag{10}$$

$$I(T^*) = \frac{N_a k_B T^*}{3\pi}\frac{v}{V_m \delta^3 \eta(T^*)} e^{-\frac{1}{k_B T^*} S(\theta)\left(-\frac{16\pi\sigma(T^*)^3}{3\Delta g_v}\right)}, \tag{11}$$

$$\sigma(T^*) = \sqrt{-\frac{k_B T^*}{8\pi}\frac{\Delta g_v ln\left[\frac{3\pi}{k_B T^*} v\delta^3 \eta(T^*)\right]}{\delta S(\theta)}}, \tag{12}$$

$$\eta(T^*) = \eta_{T_m} e^{\frac{AT_0}{T_m - T_0}\cdot\frac{T_m - T^*}{T^* - T_0}}. \tag{13}$$

The key feature of this model is the established relationship between the critical interface energy $\sigma(T^*)$ and the critical nucleation viscosity $\eta(T^*)$.[5] The temperature and time dependence of the critical nucleation viscosity $\eta(T^*)$ are shown as blue lines in the main and inset of Figure 6B, respectively. Three material-related parameters A, T_0, and $S(\theta)$ were determined by fitting experimental data from the TTT curve (T^*, t^*). In this model, A and T_0 in the critical nucleation viscosity model are intrinsic properties of the material system, while $S(\theta)$ is significantly influenced by experimental conditions. Several derived thermodynamic parameters, obtained from the quantitative analysis of the TTT curve, are listed in Table S7.

The fitting process is governed by several constraints, which include 4 experimental data points obtained from ultrafast isothermal measurements in this study, 18 additional data points in the low-temperature region from traditional measurement methods, and the high-temperature melting point that corresponds to infinite incubation time at a stable equilibrium state. Since the phenomenological model has only three unknown parameters, this combination of constraints effectively ensures the reliability of the fitting process. As shown in both Figures 6A-B, although only a limited number of ultrafast crystallization data points are available, the fitted curves capture the overall trend well and remain accurate in the nose-point region—even on a logarithmic timescale, where the fitting is most sensitive. Ultrafast and slow phase-change data together are essential for accurately shaping the overall TTT and $\eta - t$ curves, especially their extension towards lower temperatures and longer times, which affects the key parameter T_0. In other words, the accurate estimation of T_0 at the infinite-time limit is made possible by the incorporation of ultrafast data points near the nose region, which were previously unavailable.

The data near the nose point of the TTT curve, corresponding to the shortest incubation time for crystallization, are critical for fitting and determining the material properties. PCMs must exhibit rapid transition rates between crystalline and amorphous states, which are essential for device efficiency. This study demonstrates that the $Ge_2Sb_2Te_5$ nose point occurs at 8×10^{-8} s.

The parameter T_0 denotes the temperature at which the critical viscosity becomes infinite, as well as the temperature at which the critical incubation time of the TTT curve diverges to infinity, as shown separately in Figures 6A-B. T_0 serves as an effective freezing point below which atomic mobility becomes sufficiently restricted, preventing structural relaxation within experimentally accessible timescales. Recalling the fundamental question about the nature of the glassy state raised in the introduction, the transition from an amorphous liquid to an amorphous solid is traditionally defined by a quantitative change in viscosity with temperature, typically at 10^{12} or 10^{13} Pa·s as an empirical criterion.[2,3,9] In contrast, T_0 here establishes a precise thermodynamic temperature boundary, marking a qualitative transition from the amorphous liquid to the amorphous solid phase.[5] Specifically, the T_0 for $Ge_2Sb_2Te_5$ is 206.54 K, which gives a clear physical picture that the material system remains in an amorphous liquid state at room temperature with extremely limited fluidity. While atomic motion is significantly restricted, the material system retains a certain degree of configurational freedom, theoretically allowing for the possibility of crystallization. However, the critical nucleation incubation time t^* for $Ge_2Sb_2Te_5$ at room temperature is approximately 10^{33} s (10^{24} years, see Table S7), ensuring that $Ge_2Sb_2Te_5$-based phase change memory devices exhibit high thermal phase stability over extended periods.

Nevertheless, the applicability of the approach is constrained by certain limitations. The current time scale of PLIHS is limited to a sub-nanosecond scale. However, at shorter time scales, such as picoseconds and femtoseconds, non-thermal laser-induced phase transition processes may take place, which are beyond the scope of this article.[86] Moreover, the classical thermodynamic TTT curve model cannot adequately describe the multiple-nose TTT curves often observed in multi-component amorphous systems, as it fails to account for the influence of different compositions on nucleation and crystal growth.[87]

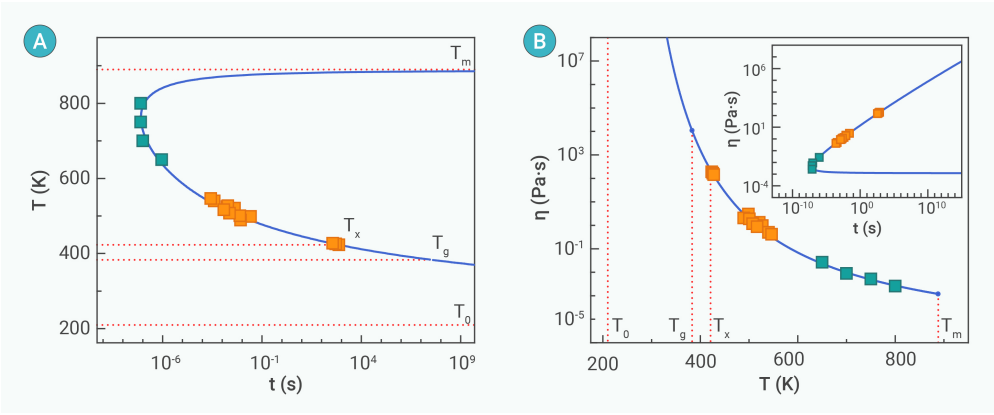

Figure 6. Critical nucleation analysis of $Ge_2Sb_2Te_5$ (A) The TTT curve for $Ge_2Sb_2Te_5$. (B) Critical nucleation viscosity as a function of temperature and time for $Ge_2Sb_2Te_5$. In both (A) and (B), data marked with yellow squares are from Ref. [19], while data marked with green squares are from this study.

CONCLUSION

In conclusion, this study developed an innovative approach for crystallization thermodynamic characterization using PLIHS and successfully applied it to $Ge_2Sb_2Te_5$ materials, addressing the gap in ultrafast TTT curve characterization. The PLIHS-based approach surpasses traditional techniques with ultrafast heating and cooling rates exceeding 10^{11} K/s. Integrated with calibrated finite element heat transfer simulations, it allows for precise control of the isothermal program and ultimately enables the characterization of the TTT curve, particularly near the nose points. Critical nucleation times below 100 ns were observed within the 650-800 K temperature range, demonstrating the rapid phase transitions of $Ge_2Sb_2Te_5$. This innovative technique offers the potential for ultrafast characterization of the thermodynamics involved in crystallization of a single phase governed by the nucleation-crystal growth mechanism and is especially crucial for electronic materials such as PCMs, facilitating advancements in thermodynamic studies for non-von Neumann ANN applications. By integrating calorimetric data, a comprehensive TTT curve is constructed, which is effectively depicted by a single phenomenological model. The analysis of the TTT curve and viscosity variation near the critical temperature T_0 reveals the atomic configuration freezing phenomenon in the glassy solid state, providing a new research tool for investigating the "nature of glassy substances".

REFERENCES

1. So Much More to Know. (2005). *Science* **309**:78-102. DOI:10.1126/science.309.5731.78b
2. Debenedetti P. G. and Stillinger F. H. (2001). Supercooled liquids and the glass transition. *Nature* **410**:259–267. DOI:10.1038/35065704
3. Gao Q. and Jian Z. (2020). Predicting the thermodynamic ideal glass transition temperature in glass-forming liquids. *Materials* **13**:2151. DOI:10.3390/ma13092151
4. Kauzmann W. (1948). The nature of the glassy state and the behavior of liquids at low temperatures. *Chem. Rev.* **43**:219–256. DOI:10.1021/cr60135a002
5. Dong H.-D., Zhang P., Qin M.-Y., et al. (2024). Quantitative understanding of the initial stage of liquid to crystalline or amorphous phase transitions. *Innov. Mater.* **2**:100086. DOI:10.59717/j.xinn-mater.2024.100086
6. Becker R. and Döring W. (1954). Kinetic treatment of the nucleation in supersaturated vapors (National Advisory Commitee for Aeronautics).
7. Jund P., Caprion D. and Jullien R. (1997). Is there an ideal quenching rate for an ideal glass. *Phys. Rev. Lett.* **79**:91–94. DOI:10.1103/PhysRevLett.79.91
8. Zhong L., Wang J., Sheng H., et al. (2014). Formation of monatomic metallic glasses through ultrafast liquid quenching. *Nature* **512**:177–180. DOI:10.1038/nature13617
9. Kawazoe Y., Yu J.-Z., Tsai A.-P., et al. (1997). Phase diagrams and physical properties of nonequilibrium alloys. Subvol. A. (ed) Nonequilibrium phase diagrams of ternary amorphous alloys (Springer). DOI:10.1007/978-3-662-64978-7
10. Mukherjee S., Zhou Z., Schroers J., et al. (2004). Overheating threshold and its effect on time–temperature-transformation diagrams of zirconium based bulk metallic glasses. *Appl. Phys. Lett.* **84**:5010–5012. DOI:10.1063/1.1763219
11. Mukherjee S., Kang H.-G., Johnson W., et al. (2004). Noncontact measurement of crystallization behavior, specific volume, and viscosity of bulk glass-forming Zr-Al-Co-(Cu) alloys. *Phys. Rev. B* **70**:174205. DOI:10.1103/PhysRevB.70.174205
12. Ericsson A., Pacheco V., Sahlberg M., et al. (2020). Transient nucleation in selective laser melting of Zr-based bulk metallic glass. *Mater. Des.* **195**:108958. DOI:10.1016/j.matdes.2020.108958
13. Kim Y. J., Busch R., Johnson W. L., et al. (1996). Experimental determination of a time–temperature - transformation diagram of the undercooled $Zr_{41.2}Ti_{13.8}Cu_{12.5}Ni_{10.0}Be_{22.5}$ alloy using the containerless electrostatic levitation processing technique. *Appl. Phys. Lett.* **68**:1057-1059. DOI:10.1063/1.116247
14. Hays C. C., Schroers J., Johnson W. L., et al. (2001). Vitrification and determination of the crystallization time scales of the bulk-metallic-glass-forming liquid $Zr_{58.5}Nb_{2.8}Cu_{15.6}Ni_{12.8}Al_{10.3}$. *Appl. Phys. Lett.* **79**:1605-1607. DOI:10.1063/1.1398605
15. Bai F. X., Yao J. H., Wang Y. X., et al. (2017). Crystallization kinetics of an Au-based metallic glass upon ultrafast heating and cooling. *Scr. Mater.* **132**:58–62. DOI:10.1016/j.scriptamat.2017.02.001
16. Löffler J. F., Schroers J. and Johnson W. L. (2000). Time–temperature–transformation diagram and microstructures of bulk glass forming $Pd_{40}Cu_{30}Ni_{10}P_{20}$. *Appl. Phys. Lett.* **77**:681–683. DOI:10.1063/1.127084
17. Legg B. A., Schroers J. and Busch R. (2007). Thermodynamics, kinetics, and crystallization of $Pt_{57.3}Cu_{14.6}Ni_{5.3}P_{22.8}$ bulk metallic glass. *Acta. Mater.* **55**:1109-1116. DOI:10.1016/j.actamat.2006.09.024
18. Marseglia E. A. and Davis E. A. (1982). Crystallization of amorphous selenium and $As_{0.005}Se_{0.995}$. *J. Non-Cryst. Solids* **50**:13-21. DOI:10.1016/0022-3093(82)90195-8
19. Zhao J., Hui J., Ye Z., et al. (2022). Exploring "no man's land"—arrhenius crystallization of thin-film phase change material at 1 000 000 k s^{-1} via nanocalorimetry. *Adv. Mater. Interfaces* **9**:2200429. DOI:10.1002/admi.202200429
20. Schroers J. (2010). Processing of bulk metallic glass. *Adv. Mater.* **22**:1566–1597. DOI:10.1002/adma.200902776
21. Kumar G., Tang H. X. and Schroers J. (2009). Nanomoulding with amorphous metals. *Nature* **457**:868–872. DOI:10.1038/nature07718
22. Peng H. L., Li M. Z. and Wang W. H. (2011). Structural signature of plastic deformation in metallic glasses. *Phys. Rev. Lett.* **106**:135503. DOI:10.1103/PhysRevLett.106.135503
23. Liu Y. H., Wang D., Nakajima K., et al. (2011). Characterization of nanoscale mechanical heterogeneity in a metallic glass by dynamic force microscopy. *Phys. Rev. Lett.* **106**:125504. DOI:10.1103/PhysRevLett.106.125504
24. Vladár K. and Zawadowski A. (1983). Theory of the interaction between electrons and the two-level system in amorphous metals. *I. Noncommutative model Hamiltonian and scaling of first order. Phys. Rev. B* **28**:1564–1581. DOI:10.1103/PhysRevB.28.1564
25. Nagel S. R. (1977). Temperature dependence of the resistivity in metallic glasses. *Phys. Rev. B* **16**:1694–1698. DOI:10.1103/PhysRevB.16.1694
26. Schawe J. E. K. and Pogatscher S. (2016). Material characterization by fast scanning calorimetry: Practice and applications. Schick C. and Mathot V. (eds). Fast scanning calorimetry, (Springer International Publishing), pp:3-80. DOI:10.1007/978-3-319-31329-0_1
27. Yi F. and LaVan D. A. (2019). Nanocalorimetry: Exploring materials faster and smaller. *Appl. Phys. Rev.* **6**:031302. DOI:10.1063/1.5098297
28. Huxtable S., Cahill D. G., Fauconnier V., et al. (2004). Thermal conductivity imaging at micrometre-scale resolution for combinatorial studies of materials. *Nat. Mater.* **3**:298–301. DOI:10.1038/nmat1114
29. Wei C., Zheng X., Cahill D. G., et al. (2013). Micron resolution spatially resolved measurement of heat capacity using dual-frequency time-domain thermoreflectance. *Rev. Sci. Instrum.* **84**:071301. DOI:10.1063/1.4815867
30. Zheng X., Cahill D. G., Weaver R., et al. (2008). Micron-scale measurements of the coefficient of thermal expansion by time-domain probe beam deflection. *J. Appl. Phys.* **104**:073509. DOI:10.1063/1.2988111
31. Zhao J.-C. (2014). High-throughput experimental tools for the materials genome initiative. *Chin. Sci. Bull.* **59**:1652–1661. DOI:10.1007/s11434-014-0120-1
32. Shin J., Gamage G. A., Ding Z., et al. (2022). High ambipolar mobility in cubic boron arsenide. *Science* **377**:437–440. DOI. DOI:10.1126/science.abn4290
33. Huberman S., Duncan R. A., Chen K., et al. (2019). Observation of second sound in graphite at temperatures above 100 K. *Science* **364**:375–379. DOI. DOI:10.1126/science.aav3548
34. Ma E., Mazzarello R. and Zhang W. (2019). Phase-change materials in electronics and photonics. *MRS Bull.* **44**:686–690. DOI:10.1557/mrs.2019.201
35. Guo P., Sarangan A. M. and Agha I. (2019). A review of germanium-antimony-telluride phase change materials for non-volatile memories and optical modulators. *Appl. Sci.* **9**:530. DOI:10.3390/app9030530
36. Wuttig M. and Yamada N. (2007). Phase-change materials for rewriteable data storage. *Nat. Mater.* **6**:824–832. DOI:10.1038/nmat2009
37. Sebastian A., Le Gallo M. and Eleftheriou E. (2019). Computational phase-change memory: Beyond von Neumann computing. *J. Phys. D: Appl. Phys.* **52**:443002. DOI:10.1088/1361-6463/ab37b6
38. Sevison G. A., Farzinazar S., Burrow J. A., et al. (2020). Phase change dynamics and two-dimensional 4-bit memory in $Ge_2Sb_2Te_5$ via telecom-band encoding. *ACS Photonics* **7**:480–487. DOI:10.1021/acsphotonics.9b01456
39. Tong X., Zhang Y.-E., Shang B.-S., et al. (2024). Breaking the vitrification limitation of monatomic metals. *Nat. Mater.* **23**:1193–1199. DOI:10.1038/s41563-024-01967-0
40. Huang H., Zuo F., Zhai F., et al. (2009). Fast phase transition process of $Ge_2Sb_2Te_5$ film induced by picosecond laser pulses with identical fluences. *J. Appl. Phys.* **106**. DOI:10.1063/1.3222851.
41. Kiselev A. V., Ionin V. V., Burtsev A. A., et al. (2022). Dynamics of reversible optical properties switching of $Ge_2Sb_2Te_5$ thin films at laser-induced phase transitions. *Opt. Laser Technol.* **147**:107701. DOI:10.1016/j.optlastec.2021.107701
42. Liu Y., Aziz M. M., Shalini A., et al. (2012). Crystallization of $Ge_2Sb_2Te_5$ films by

amplified femtosecond optical pulses. *J. Appl. Phys.* **112**:123526. DOI:10.1063/1.4770359.
43. Du J., Zhou J., Zhang L., et al. (2022). Investigation of the crystallization characteristics of intermediate states in $Ge_2Sb_2Te_5$ thin films induced by nanosecond multi-pulsed laser irradiation. *Nanomaterials* **12**:536. DOI:10.3390/nano12030536
44. Liu F. R., Han X. X., Bai N., et al. (2014). Numerical simulation on the temperature field induced by a nanosecond pulsed excimer laser in the phase-change film. *Thin Solid Films* **551**:102–109. DOI:10.1016/j.tsf.2013.11.092
45. Xiang X.-D., Wang G., Zhang X., et al. (2015). Individualized pixel synthesis and characterization of combinatorial materials chips. *Engineering* **1**:225–233. DOI:10.15302/J-ENG-2015041
46. Weidenhof V., Friedrich I., Ziegler S., et al. (2001). Laser induced crystallization of amorphous $Ge_2Sb_2Te_5$ films. *J. Appl. Phys.* **89**:3168–3176. DOI:10.1063/1.1351868
47. Němec P., Nazabal V., Moreac A., et al. (2012). Amorphous and crystallized Ge–Sb–Te thin films deposited by pulsed laser: Local structure using Raman scattering spectroscopy. *Mater. Chem. Phys.* **136**:935–941. DOI:10.1016/j.matchemphys.2012.08.024
48. Yalon E., Deshmukh S., Muñoz Rojo M., et al. (2017). Spatially resolved thermometry of resistive memory devices. *Sci. Rep.* **7**:15360. DOI:10.1038/s41598-017-14498-3
49. Burtsev A. A., Eliseev N. N., Mikhalevsky V. A., et al. (2022). Physical properties' temperature dynamics of GeTe, $Ge_2Sb_2Te_5$ and $Ge_2Sb_2Se_4Te_1$ phase change materials. *Mater. Sci. Semicond. Process.* **150**:106907. DOI:10.1016/j.mssp.2022.106907
50. Giraud V., Cluzel J., Sousa V., et al. (2005). Thermal characterization and analysis of phase change random access memory. *J. Appl. Phys.* **98**:013520. DOI:10.1063/1.1944910.
51. Guo T., Song S., Song Z., et al. (2018). SiC-doped $Ge_2Sb_2Te_5$ phase-change material: A candidate for high-density embedded memory application. *Adv. Electron. Mater.* **4**:1800083. DOI:10.1002/aelm.201800083
52. Zhang Q., Lian C., Xu Q., et al. (2023). Density of amorphous sputtered $Ge_2Sb_2Te_5$ thin films. *AIP Adv.* **13**. DOI:10.1063/5.0133477.
53. Ulbricht R., Hendry E., Shan J., et al. (2011). Carrier dynamics in semiconductors studied with time-resolved terahertz spectroscopy. *Rev. Mod. Phys.* **83**:543–586. DOI:10.1103/RevModPhys.83.543
54. Uemura Y., Kido D., Wakisaka Y., et al. (2016). Dynamics of photoelectrons and structural changes of tungsten trioxide observed by femtosecond transient XAFS. *Angew. Chem. Int. Ed.* **55**:1364–1367. DOI:10.1002/anie.201509252
55. Obara Y., Ito H., Ito T., et al. (2017). Femtosecond time-resolved X-ray absorption spectroscopy of anatase TiO_2 nanoparticles using XFEL. *Struct. Dynam.* **4**:044033. DOI:10.1063/1.4989862
56. Pecha R., Gompf B., Nick G., et al. (1998). Resolving the sonoluminescence pulse shape with a streak camera. *Phys. Rev. Lett.* **81**:717–720. DOI:10.1103/PhysRevLett.81.717
57. van der Geest M. L. S., Sadegh N., Meerwijk T. M., et al. (2021). Extreme ultraviolet-excited time-resolved luminescence spectroscopy using an ultrafast table-top high-harmonic generation source. *Rev. Sci. Instrum.* **92**:113004. DOI:10.1063/5.0064780
58. Liang J. and Wang L. V. (2018). Single-shot ultrafast optical imaging. *Optica* **5**:1113–1127. DOI:10.1364/OPTICA.5.001113
59. Le H., Penchev P., Henrottin A., et al. (2020). Effects of top-hat laser beam processing and scanning strategies in laser micro-structuring. *Micromachines* **11**:221. DOI:10.3390/mi11020221
60. Homburg O. and Mitra T. (2012). Gaussian-to-top-hat beam shaping: an overview of parameters, methods, and applications. *Laser Resonators, Microresonators, and Beam Control XIV* **8236**:62–70. DOI:10.1117/12.907914
61. Yamada N., Ohno E., Nishiuchi K., et al. (1991). Rapid - phase transitions of GeTe - Sb_2Te_3 pseudobinary amorphous thin films for an optical disk memory. *J. Appl. Phys.* **69**:2849–2856. DOI:10.1063/1.348620
62. Ohta T., Inoue K., Uchida M., et al. (1989). Phase change disk media having rapid cooling structure. *Jpn. J. Appl. Phys.* **28**:123. DOI:10.7567/JJAPS.28S3.123
63. Kalb J., Spaepen F. and Wuttig M. (2003). Calorimetric measurements of phase transformations in thin films of amorphous Te alloys used for optical data storage. *J. Appl. Phys.* **93**:2389–2393. DOI:10.1063/1.1540227
64. Lee J., Bozorg-Grayeli E., Kim S., et al. (2013). Phonon and electron transport through $Ge_2Sb_2Te_5$ films and interfaces bounded by metals. *Appl. Phys. Lett.* **102**:191911. DOI:10.1063/1.4807141
65. Kuwahara M., Suzuki O., Yamakawa Y., et al. (2007). Temperature dependence of the thermal properties of optical memory materials. *Jpn. J. Appl. Phys.* **46**:3909. DOI:10.1143/JJAP.46.3909
66. Lambert J.-H. (1760). Photometria sive de mensura et gradibus luminis, colorum et umbrae (Eberhardt Klett)
67. Lurie M. V. (2008). Modeling of oil product and gas pipeline transportation (Wiley VCH Verlag). DOI:10.1002/9783527626199
68.
69. Njoroge W. K., Wöltgens H.-W. and Wuttig M. (2002). Density changes upon crystallization of $Ge_2Sb_{2.04}Te_{4.74}$ films. *J. Vac. Sci. Technol. A* **20**:230-233. DOI:10.1116/1.1430249
70. Weidenhof V., Friedrich I., Ziegler S., et al. (1999). Atomic force microscopy study of laser induced phase transitions in $Ge_2Sb_2Te_5$. *J. Appl. Phys.* **86**:5879–5887. DOI:10.1063/1.371606
71. Kuwahara M., Suzuki O., Yamakawa Y., et al. (2007). Measurement of the thermal conductivity of nanometer scale thin films by thermoreflectance phenomenon. *Microelectron. Eng.* **84**:1792–1796. DOI:10.1016/j.mee.2007.01.178
72. Battaglia J.-L., Kusiak A., Schick V., et al. (2010). Thermal characterization of the SiO_2-$Ge_2Sb_2Te_5$ interface from room temperature up to 400°C. *J. Appl. Phys.* **107**:044314. DOI:10.1063/1.3284084
73. Lee J., Li Z., Reifenberg J. P., et al. (2011). Thermal conductivity anisotropy and grain structure in $Ge_2Sb_2Te_5$ films. *J. Appl. Phys.* **109**:084902 . DOI:10.1063/1.3573505
74. Aryana K., Zhang Y., Tomko J. A., et al. (2021). Suppressed electronic contribution in thermal conductivity of $Ge_2Sb_2Se_4Te$. *Nat. Commun.* **12**:7187. DOI:10.1038/s41467-021-27121-x
75. Reifenberg J. P., Panzer M. A., Kim S., et al. (2007). Thickness and stoichiometry dependence of the thermal conductivity of GeSbTe films. *Appl. Phys. Lett.* **91**. DOI:10.1063/1.2784169
76. Risk W. P., Rettner C. T. and Raoux S. (2008). In situ 3ω techniques for measuring thermal conductivity of phase-change materials. *Rev. Sci. Instrum.* **79**:026108 . DOI:10.1063/1.2841802
77. Risk W. P., Rettner C. T. and Raoux S. (2009). Thermal conductivities and phase transition temperatures of various phase-change materials measured by the 3ω method. *Appl. Phys. Lett.* **94**:101906. DOI:10.1063/1.3097353
78. Lee D., Yim S.-S., Lyeo H.-K., et al. (2010). Formation of $Ge_2Sb_2Te_5$ – TiO_x nanostructures for phase change random access memory applications. *Electrochemical and Solid-State Letters* **13**:K8. DOI:10.1149/1.3264734
79. Lee J., Kim S., Jeyasingh R., et al. (2011). Microthermal stage for electrothermal characterization of phase-change memory. *IEEE Electron Device Lett.* **32**:952–954. DOI:10.1109/LED.2011.2144952
80. Aryana K., Kim H. J., Islam M. R., et al. (2023). Optical and thermal properties of $Ge_2Sb_2Te_5$, Sb_2Se_3, and Sb_2S_3 for reconfigurable photonic devices. *Opt. Mater. Express* **13**:3277–3286. DOI:10.1364/OME.503178
81. Aryana K., Gaskins J. T., Nag J., et al. (2021). Interface controlled thermal resistances of ultra-thin chalcogenide-based phase change memory devices. *Nat. Commun.* **12**:774. DOI:10.1038/s41467-020-20661-8
82. Orava J., Greer A. L., Gholipour B., et al. (2012). Characterization of supercooled liquid $Ge_2Sb_2Te_5$ and its crystallization by ultrafast-heating calorimetry. *Nat. Mater.* **11**:279–283. DOI:10.1038/nmat3275
83. Turnbull D. (1962). On the relation between crystallization rate and liquid structure. *J. Phys. Chem.* **66**:609–613. DOI:10.1021/j100810a009
84. Turnbull D. and Fisher J. C. (1949). Rate of nucleation in condensed systems. *J. Chem. Phys.* **17**:71–73. DOI:10.1063/1.1747055
85. Garca-Coln L. S., del Castillo L. F. and Goldstein P. (1989). Theoretical basis for the Vogel-Fulcher-Tammann equation. *Phys. Rev. B* **40**:7040–7044. DOI:10.1103/PhysRevB.40.7040
86. Sundaram S. K. and Mazur E. (2002). Inducing and probing non-thermal transitions in semiconductors using femtosecond laser pulses. *Nat. Mater.* **1**:217–224. DOI:10.1038/nmat767
87. Lu Z. P., Ma D., Liu C. T., et al. (2007). Competitive formation of glasses and glass–matrix composites. *Intermetallics* **15**:253–259. DOI:10.1016/j.intermet.2006.05.015

FUNDING AND ACKNOWLEDGMENTS

We would like to acknowledge the Major Science and Technology Infrastructure Project of Material Genome Big-science Facilities Platform supported by the Municipal Development and Reform Commission of Shenzhen. This work was supported by the Shenzhen Science and Technology Innovation Commission (Grant Nos. JCYJ20240813095259010, JCYJ20241202123919027, JCYJ20220818100613028 and JCYJ20220530112816038). The founders had no role in study design, data collection and analysis, decision to publish, or preparation of the manuscript.

AUTHOR CONTRIBUTIONS

X.-D.X proposed and conceived the project. X.-D.X and M.S. designed the experiments. M.S. and M.-X.C. constructed the PLIHS and prepared the film sample. P.Z. and H.-D.D. performed theoretical simulations, calculations and experiments. M.-Y.Q. made important suggestions and assisted in improving the manuscript. H.-D.D., M.-X.C., M.S. and X.-D.X. wrote the manuscript with input from all authors. All authors contributed to the manuscript and approved the final version

DECLARATION OF INTERESTS

The authors declare no competing interests.

DATA AND CODE AVAILABILITY

Data underlying the results presented in this paper are not publicly available at this time but are available from the authors upon reasonable request.

SUPPLEMENTAL INFORMATION

It can be found online at https://doi.org/10.59717/j.xinn-mater.2025.100163

LEAD CONTACT WEBSITE

X.-D. Xiang, https://people.ucas.ac.cn/~0082938